The Astrophysical Journal Letters, 878:L15 (7pp), 2019 June 10 https://doi.org/10.3847/2041-8213/ab2330

Spectral Diagnosis of Mg II and Hα Lines during the Initial Stage of an M6.5 Solar Flare

Nengyi Huang[1,2], Yan Xu[1,2], Viacheslav M Sadykov[3], Ju Jing[1,2], and Haimin Wang[1,2]
[1] Center for Solar-Terrestrial Research, Institute of Space Weather Science, New Jersey Institute of Technology, 323 Martin Luther King Boulevard, Newark, NJ 07102, USA
[2] Big Bear Solar Observatory, New Jersey Institute of Technology, 40386 North Shore Lane, Big Bear, CA 92314, USA
[3] Center for Computational Heliophysics, Institute for Space Weather Sciences, New Jersey Institute of Technology, 323 Martin Luther King Boulevard, Newark, NJ 07102, USA
Received 2019 January 7; revised 2019 May 20; accepted 2019 May 20; published 2019 June 7

Abstract

Recent studies have shown special spectral properties during the initial stage of flare emissions, such as the enhanced absorption in He I 10830 Å line and a strong redshift in Hα. Using the high-resolution imaging spectroscopic data obtained by the *Interface Region Imaging Spectrograph* (*IRIS*), we investigate the Mg II emission lines during an M6.5 flare (SOL2015-06-22T18:23), which was well covered by the joint observation of *IRIS* and the Goode Solar Telescope at Big Bear Solar Observatory. On the leading edge of the propagating ribbon, Mg II lines are characterized by blue-wing enhancement and strong broadening. On the other hand, redshifts in Mg II and Hα are found in the trailing areas of the flare ribbons. Numerical modeling, produced by combining RADYN and RH, suggests that the Mg II line broadening is possibly caused by unresolved turbulence with velocities about 10 to 30 km s^{-1}. The enhanced blue wing is likely due to a decrease of temperature and an increase of electron density, as consequences of electron precipitation. Based on the observations and simulation results, we discuss the possible response of the lower atmosphere to the electron precipitation, in terms of the evolution of temperature, electron density, and turbulence velocities.

Key words: Sun: activity – Sun: chromosphere – Sun: flares

1. Introduction

Flare footpoints are usually ribbon-like structures at lower atmospheres. The intensities over the ribbon are not uniform with high-resolution observations. For instance, core-halo structures can be found on the well-defined white-light ribbons. Xu et al. (2006) and Isobe et al. (2007) explained these features using dual-heating mechanisms, namely direct heating and chromospheric backwarming. Benefiting from the improvement of modern instruments, unprecedented resolutions have revealed finer structures. The 1.6 m Goode Solar Telescope at Big Bear Solar Observatory (BBSO/GST; Goode & Cao 2012) currently provides the highest resolution at visible (0.″027 pix^{-1}) and near-infrared (NIR) wavelengths. Sharykin & Kosovichev (2014) and Jing et al. (2016) found 100–160 km narrow leading frontier that shows strong pseudo-redshifts in Hα line. Xu et al. (2016) reported enhanced absorption in He I 10830 Å, concentrated in a 34-km-wide ribbon front. More importantly, this absorption is co-aligned with strongly broadened Mg II line profiles with an FWHM of 1 Å observed by the *Interface Region Imaging Spectrograph* (*IRIS*; De Pontieu et al. 2014). Panos et al. (2018) implemented machine learning method on 33 flares and found universal characteristics on leading ribbon fronts, including strong broadening, blueshift, and central reversal. According to the standard flare model, the leading front of the ribbon represents the footpoints of the newly reconnected flare loops. Therefore, the different characteristics on the leading front and trailing areas indicate the difference of distributions in the initial precipitating electron beam and the trapped electrons by the magnetic loops.

In addition to emissions, other signatures of precipitating electrons, chromospheric evaporation and condensation (Fisher et al. 1985), have been observed and studied using coronal (Graham et al. 2011; Milligan 2015) and chromospheric lines (Canfield et al. 1990). The evaporation speed reaches 300 km s^{-1} and the condensation speed can reach 40 km s^{-1} (Graham et al. 2011; Graham & Cauzzi 2015). On the other hand, the existence of the dominant stationary component suggests that the observed Doppler signals come from multiple filamentary loops (Harrison et al. 1995). Falchi et al. (1997) found that chromospheric condensation was concentrated at the leading front of a flaring ribbon, in agreement with the filamentary scenario indicating a relationship with the special properties of leading ribbon front. Graham & Cauzzi (2015) studied Fe XXI and Mg II lines and found that the condensation occurred earlier than the evaporation flows. More recently, Tei et al. (2018) reported blueshifted Mg II h&k lines during the impulsive phase of a flare.

In this study, we analyze the *IRIS* Mg II imaging-spectroscopic data and make a comparison with Hα pseudo-Doppler maps taken by BBSO/GST. These lines are formed in chromosphere (Wang et al. 1998; Tian et al. 2014), where evaporation and condensation originate. With high-resolution data provided by *IRIS* and BBSO/GST, important constraints of chromospheric dynamics are investigated.

2. Observations

An M6.5 flare was observed on 2015 June 22 by the joint observation of BBSO/GST and *IRIS*. The hosting active region NOAA 12371 was close to the disk center around N13W14. It started at 17:39 UT and decayed slowly over several hours. The flaring areas include an intensive core and a significantly extended region (see Jing et al. 2017). The field of view (FOV) of GST observations covered the core region of two major

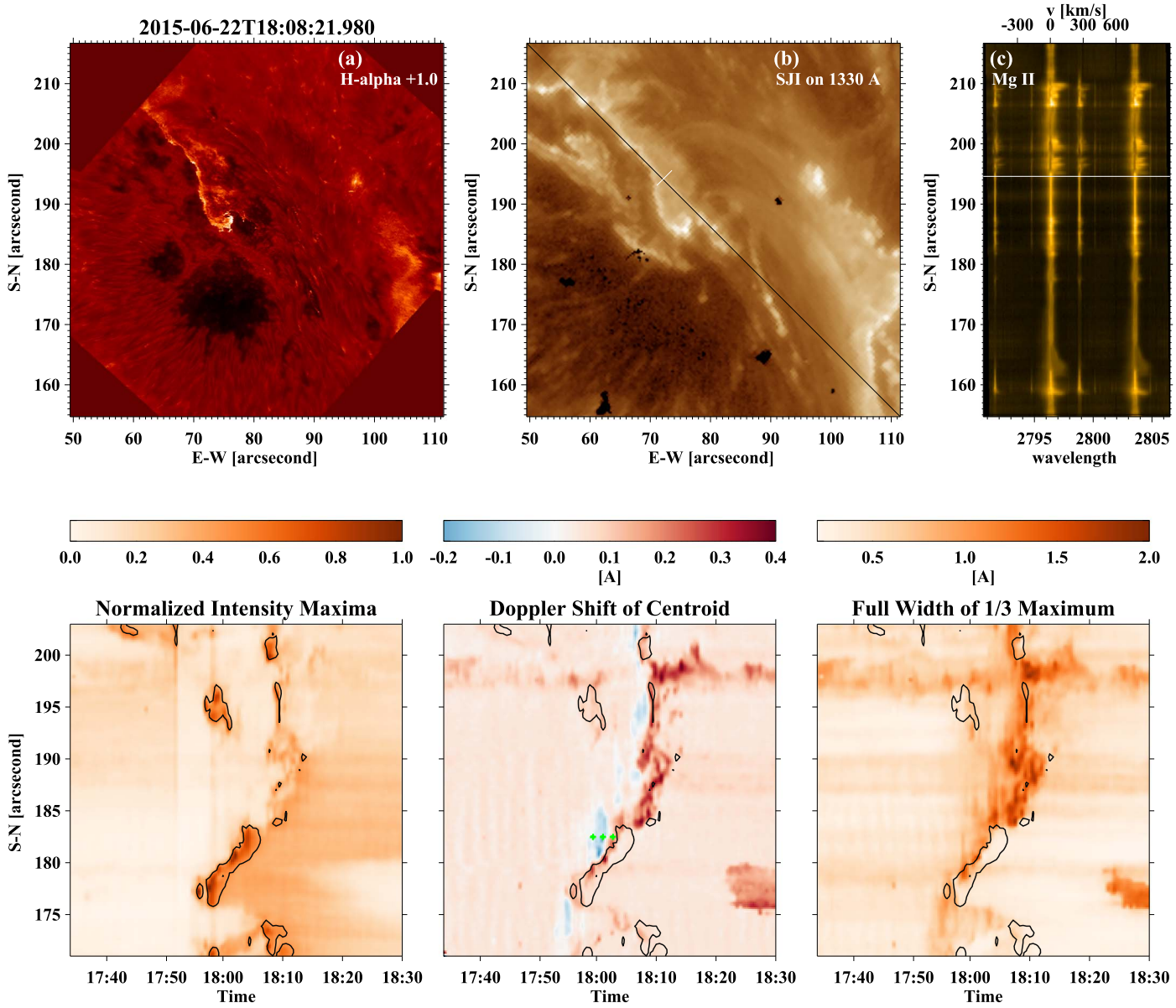

Figure 1. Panel (a): Hα off-band image taken at 18:08 UT on 2015 June 22. Panel (b): *IRIS* 1330 Å SJI within the same FOV as Hα image, the black line denotes the slit, and the short white stick marks the location of the sampling pixel mentioned in Section 3.1. Panel (c): the Mg II spectra along the slit. Lower panels: time-space diagram of emission maximum, Doppler shift of centroid, and the full width of one-third maximum of Mg II k line with corresponding color bars on top, respectively. The contours of the time-space diagram of intensity maximum are overplotted onto the diagrams of Doppler shifts and line width. The green crosses mark are representing for the data points whose line profiles are used as examples in lower panels in Figure 2.

sunspots in opposite polarities. Within this area, two flare ribbons are seen moving away from each other.

IRIS provides spectral data on far-ultraviolet (FUV; 1331.7 Å–1358.4 Å and 1389.0 Å–1407.0 Å) and near-ultraviolet (NUV; Interface 2782.7 Å–2851.1 Å), as well as the slit-jaw images (SJIs; taken at 1330 Å, 1400 Å, 2796 Å, and 2832 Å). Raster mode of large coarse 16-step and $16'' \times 130''$ FOV were used with standard flare line list (OBSID3660100039). The time lag between steps is 2 s and the cadence between scans (16 positions) is 33 s. The pixel resolution is $0\farcs6$. In this event, the *IRIS* FOV is tilted by 45° for better coverage of ribbons. Figure 1 shows sample images of GST Hα off-band and 1330 Å SJI. The spectra in panel (c) is taken along the dark slit shown in panel (b).

GST provides three channels at TiO 7057 Å, Hα, and vector magnetograms using the NIR 1.56 μm line. Weak white-light emissions were detected in the TiO band (Huang et al. 2018). In this study, we focus on the Hα images, taken at five different spectral points: center line and off-bands ($\pm$0.6 Å and $\pm$1.0 Å; see details in Jing et al. 2016). The cadence of the five-point scan is 28 s after speckle reconstruction. For the Doppler image pairs, the time lag is 3 to 4 s between the off-band image pairs. The pixel size of the Hα image is $0\farcs03$ and the FOV is $57'' \times 64''$.

In addition, context data of hard X-ray (HXR) and full-disk ultraviolet (UV) images are obtained from *Reuven Ramaty High Energy Solar Spectroscopic Imager* (*RHESSI*; Lin et al. 2002) and Atmospheric Imaging Assembly (AIA; Lemen et al. 2012) on board the *Solar Dynamic Observatory* (*SDO*; Pesnell et al. 2012), respectively. *RHESSI* data is used to extract the HXR spectral parameters, such as power-law index, low-energy cutoff, and total electron flux, which are key inputs for

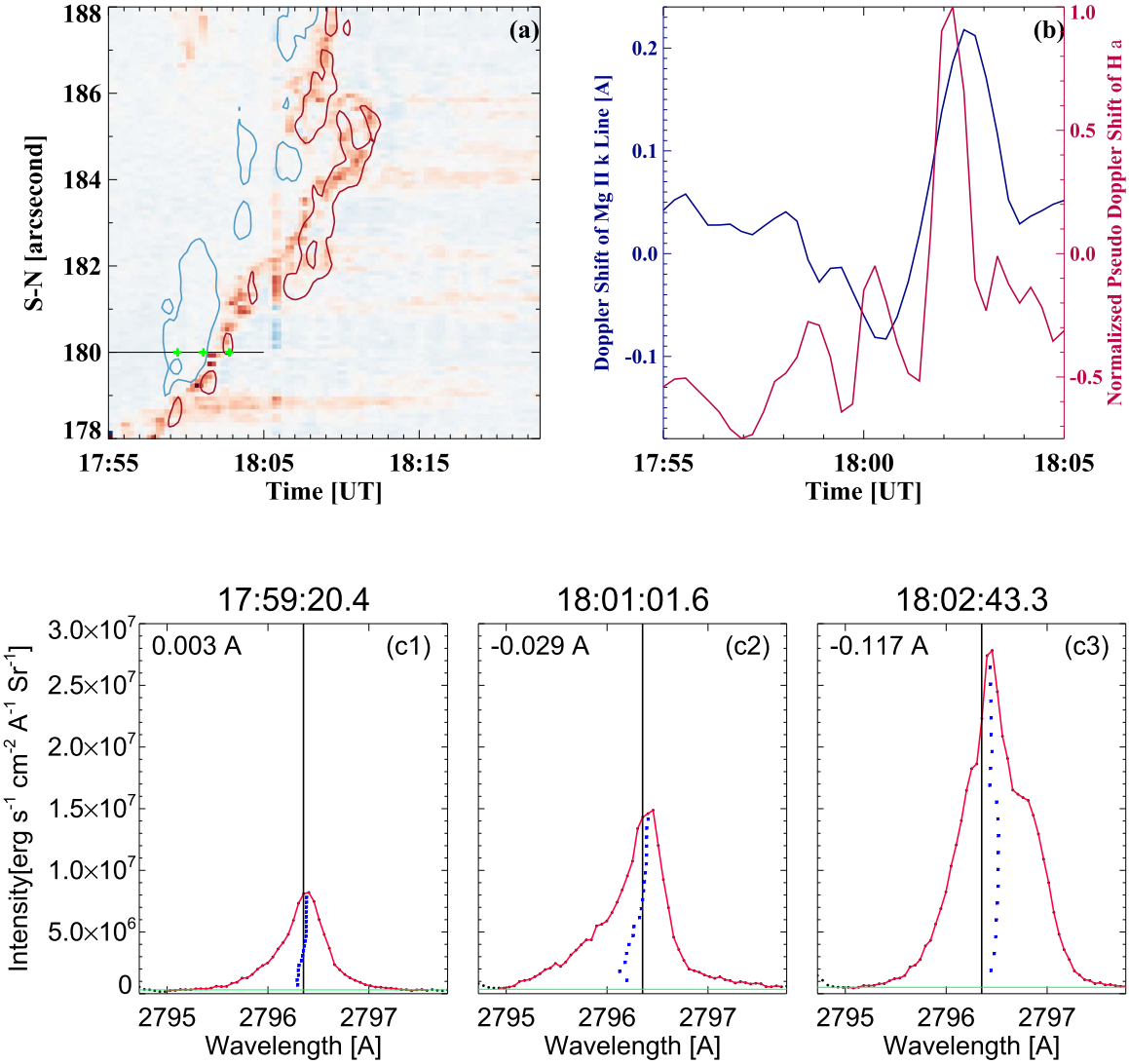

Figure 2. Panel (a): time-space diagram of Hα pseudo-Doppler shift with contours of *IRIS* Mg II k velocity (20 km s^{-1} level). The blue and red colors indicate the blue and redshift in Hα. Panel (b): temporal profiles of Mg II k line (blue) and normalized pseudo-Doppler of Hα (red). The corresponding location and time are indicated by the black line in panel (a). Panels (c1)–(c3): sample Mg II k line profiles at the initiation time (c1), with blue-wing enhancement (c2), and at flare peak (c3). The green horizontal line is the background level and the blue asterisk points are the bisectors on different intensity levels. The shifting of their centroids are on the upper-left corner of each plot.

numerical simulations. *SDO*/AIA images are used as reference images to align *IRIS* with GST data.

3. Data Analysis and Results

3.1. Mg II Blueshift and Broadening

Formed mainly in the upper chromosphere, the Mg II h&k resonance doublets are among the strongest emission lines in UV spectra. Figure 1 shows a sample spectra of Mg II lines in the range of λ2790.65 Å–λ2806.54 Å. Due to their similar behaviors, our investigation focuses on the k line at λ2796 Å. The intensity maximum, Doppler shift, and line width are measured. The line width is defined as the full width at one-third maximum (see Ding et al. 1995). To describe the line shifting, two methods are used, namely integrated centroid and bisector of different intensity levels. The centroid method is to find the difference between the integrated arithmetic mean of the line profile and the theoretical line center. The bisector method calculates the arithmetic mean at a given intensity level, for instance at the one-third maximum. The bisector shifts vary as a function of intensity levels. We found the results from one-third maximum bisector and integrated method are in good agreement.

The *IRIS* slits covered the main section of the north ribbon. Due to the similarity, the spectra at the first list position (from 16 positions) are used as the representative spectra. Time-space diagrams of the intensity maxima, Doppler shift of centroid, and full width at one-third maximum are shown in the lower panels of Figure 1. To show the evolution of the line profile more clearly, contours of intensity maxima are overlaid. From these diagrams we found the following. (1) The maximum Mg II k emission correlated with strong redshift well. (2) This line is significantly broadened over 1.0 Å at one-third maximum. (3) Blue-wing enhancement was found at 33–165 s prior to the maximum emission. The typical blueshift (averaging the entire profile) is less than 10 km s^{-1}, but can reach 20 km s^{-1} at certain locations.

Samples of Mg II k profiles are shown in the bottom of Figure 2. The time steps of these profiles are indicated by green crosses in the Doppler time-space diagram (see Figure 1). The bisector centroids at different intensity levels are shown as blue asterisks. The overall Doppler shift is calculated by averaging all of the centroids and is noted in the upper-left corner of each panel. Before being heated, the overall shift is nearly zero compared with the theoretical line center (panel (c1)). When the ribbon front passes through the second green cross, the blue-wing of the Mg II enhanced leading to a left-shift of the line centroid. Shortly after that, the ribbon with peak intensity steps in and the line profile becomes redshifted.

3.2. Hα Redshift

To investigate the spatial relationship between Mg II and Hα observations, precise image alignment is required. Both *IRIS* SJI in 1330 Å and Hα images are registered with a full-disk reference image taken in 1700 Å by *SDO*/AIA, and heliocentric coordinates of *IRIS* and GST's FOVs are determined. As shown in Figure 1, GST's FOV is well covered by the relatively larger FOV of *IRIS*. Hα pseudo-Doppler shift is calculated by subtracting blue-wing images from the red-wing images, along the *IRIS* slit positions. Panel (a) in Figure 2 shows the time-space diagram of Hα pseudo-Doppler shift, with contours of Mg II Doppler shifts. Strong Hα redshift is located between the areas with Mg II blue-wing and red-wing shifts. Since this flare ribbon moves across the slit, the relative locations represent the order of appearance of these Doppler shifts. The results indicate that the Mg II blue-wing enhanced first, followed by the redshifts in Hα and Mg II. Panel (b) plots the time profiles of Mg II k and Hα pseudo-Doppler shift at a representative location indicated by the black line in panel (a). Comparing the temporal evolution described in Wang et al. (2017), this blue-wing enhancement followed the second flare precursor, by which the conditions, such as temperature and density, of the chromosphere have been disturbed.

3.3. Numerical Modeling and Possible Physics of Doppler Signals

We attempt to explain the thermodynamic conditions of the atmosphere where Doppler signals were generated. There are several existing packages in modeling flaring atmosphere. RADYN (Carlsson & Stein 1992, 1997; Allred et al. 2005, 2015) calculates the time-dependent atmospheric response to energy deposition, capturing the dynamics of the processes. It considers optically thick radiation and calculates for the dominating atoms in chromospheric radiation-energy balance. However, Mg II was not included in the RADYN code that we use. On the other hand, the radiation transfer code, RH (Uitenbroek 2001), models the flare emissions time independently. It is possible to solve Mg II using partial frequency redistribution (PRD) instead of complete frequency redistribution (CRD) used in RADYN, which is considered to be effective in the formation of Mg II (Leenaarts et al. 2013; Sukhorukov & Leenaarts 2017). Following the idea of Rubio da Costa et al. (2016), we started with *RHESSI* HXR spectral parameters and obtained results from RADYN simulation, including parameters of the heated atmosphere, such as the temperature, velocity, electron density, and microturbulence as functions of column mass. Then these parameters are passed through RH code to calculate the Mg II profiles.

The key inputs of RADYN include energy flux, power-law index, and low-energy cutoff of nonthermal electron, obtained by fitting the *RHESSI* HXR spectra with thick target model. An HXR spectrum was generated using the default combination of front RMCs, 1, 3, 4, 5, 6, 8, and 9 in *RHESSI* GUI, before the flare peak at 17:42:28 UT. The power-law index is 5.2 and the lower cutoff energy is 20.6 KeV. Using GST (for ribbon width) and *SDO*/AIA (for ribbon length) data, the area of flare ribbons is estimated to be 5×10^{17} cm^2 and the derived electron energy flux is 10^{11} erg cm^{-2} s^{-1}. Thanks to the work done and published by F-CHROMA (http://www.fchroma.org/) project, RADYN results were ready for use.

According to the HXR parameters described above, we chose the closest available model in the F-CHROMA database with the spectral index of 5 and lower cutoff energy of 20 keV. A total flux of 10^{12} erg cm^{-2} was deposited during 20 seconds with a triangular temporal profile (i.e., the peak flux is 10^{11} erg cm^{-2} s^{-1}), and the computation covers 50 s with output at every 0.1 s. The corresponding atmosphere snapshot from F-CHROMA (RADYN output) was then used as the input of RH code. The entire atmosphere is involved and the RH model was initiated with the microturbulence velocity set to zero. In particular, we activated the *atoms/MgII_hk_PRD.atom* in the RH package, including four levels (one 3S level, two 3P levels, and the Mg III ground level), two lines, and three bound-free transitions, for preparing the atom input for RH. In addition, *H_6.atom* was set as active and *C.atom*, *O.atom*, *Si. atom* were set as passive. Figure 3 shows the simulated Mg II k line for the moment right before (red) and during (blue) the time when the enhance blue wing appeared, at $t = 7.5$ s and $t = 8.9$ s, respectively. We attempted to determine the parameters that make the observed blue-wing enhancement and broadening possible. As shown in Figure 3, a thin layer in the upper chromosphere with column mass of 10^{-4}–10^{-3} g cm^{-2} is around 10^4 K, the typical formation temperature of the Mg II line. Compared with the previous time step (red curves), the atmosphere condition varies significantly when the blueshift is seen. In particular, the electron density increased by 1.5–2 times and velocity field increased over 4 times, but the change of temperature is minor. This indicates a nonthermal process plausibly caused by precipitating electrons.

One additional adjustment is the microturbulence with velocity V_{turb},, suggested by (Rubio da Costa et al. 2016). Figures 4(a)–(c) show three Mg II profiles with V_{turb}, of 10/20/30 km s^{-1}, and the weighted combination of these profiles is shown in the last panel (blue), showing similar broadening as the observed profile (red). Because there may be multiple drives for line broadening, the above are considered to be the upper limit of the microturbulence velocity. On the other hand, the strong microturbulence removes the blue "bumps" and converts it into the blue-wing enhancement, which matches the observation. Other parameters that can cause shift and broadening were suggested by previous studies (Rubio da Costa et al. 2016; Rubio da Costa & Kleint 2017), such as the electron density. It is "pre-determined" by the RADYN results and therefore not considered in this study. Note that the modeled intensity could be several times stronger than the observations (Rubio da Costa et al. 2016), or even an order of magnitude higher. But the broadening and Doppler shifts usually match better and are more instructive. We multiplied the intensity of observed profile by 50 to scale it to the same level of the simulated profile.

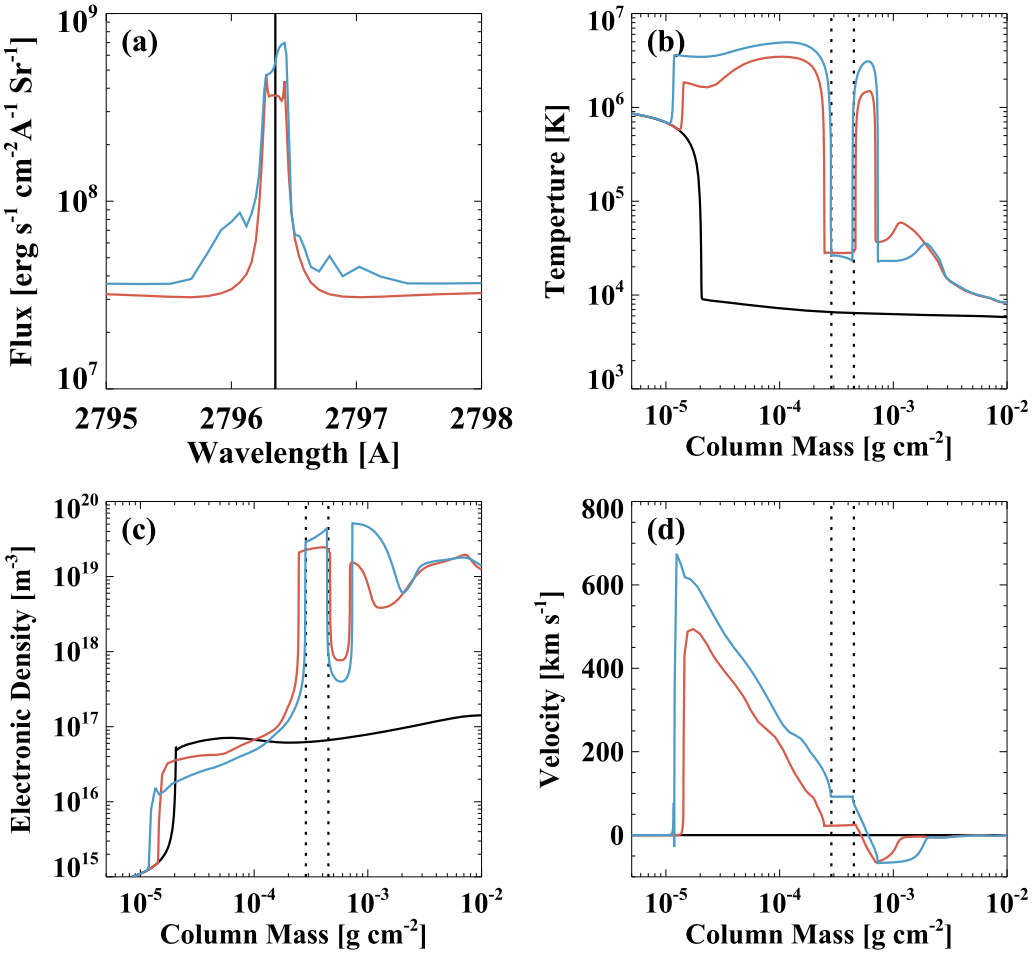

Figure 3. Simulation results from RADYN plus RH. Panel (a): modeled Mg II k line at the initiation period (red), and with blue-wing enhancement (blue). Panels (b)–(d): RADYN outputs of atmosphere snapshots as inputs for RH code, in temperature, local electron density, and velocity, as functions of column density (height), respectively. Mg II lines are formed within the height range indicated by the vertical dotted lines.

In addition, Hα line profiles are extracted directly from the RADYN output. The modeled profiles at different times are shown in the left panel of Figure 5. Kuridze et al. (2015) studied the Doppler asymmetries in Hα and suggested multiple Doppler components to fit the observed Hα profile. Our Hα observations provide five spectral points and a comprehensive comparison to modeling that is not realistic. Therefore, we construct similar pseudo-Doppler signals using ± 1.0 Å data from the simulation. The temporal variation of the pseudo-Doppler signals is plotted in the right panel of Figure 5. The red and blue vertical sticks mark the timing corresponding to the red and blue plots in Figure 3, at $t = 7.5$ s and $t = 8.9$ s, when the Mg II lines wings are in symmetry and have blue-wing enhancement, respectively. The Mg II blue-wing enhancement occurred shortly before the extremely strong redshift signal of Hα. These evolutions agree with the observations shown in Figure 2.

4. Summary and Discussion

This study presents observations of an M6.5 flare on 2015 June 22, obtained by *IRIS* and BBSO/GST. Blue asymmetry of the Mg II lines is seen prior to the typically observed redshifts in Hα and Mg II lines. Numerical modeling by RH, using the results from RADYN, suggests that the broadening is caused by spatially unresolved microturbulence, with velocities from 10 to 30 km s^{-1}. This is consistent with one of the possible mechanisms discussed in Tei et al. (2018). Strong redshifts are seen in the modeled Hα pseudo-Doppler diagram occurring after Mg II blueshift, which agrees with the observations.

The blue-wing enhancement in Mg II k line is likely due to the increase of local electron density and velocity field in the atmospheric layer that emits Mg II radiation. We construct a possible physical picture to explain the reaction of the lower atmosphere to the precipitating electrons. At the initial stage of the flare, following the second precursor of the flare, energetic electrons propagate downward and stop at the chromosphere. Consequently, the atmosphere around the precipitation site is heated from 10^4 to 10^6 K and the electron density increases continuously, leading to an expansion of this layer both upward and downward. This layer is then quickly cooled down to 10^4 K, which is favorable for the production of Mg II lines. Because of the higher density in the lower layers, the downward expansion is slow and weak. Therefore, a broadened Mg II profile is seen with the blue wing more enhanced. The downward propagation of heating compresses the lower layer where Hα formed. A strong redshift of Hα is observed as a consequence of condensation. When the plasma reached the balance, the momentum deposit by the accelerated electron beam dominated and the downward plasma produced the following Mg II lines redshift.

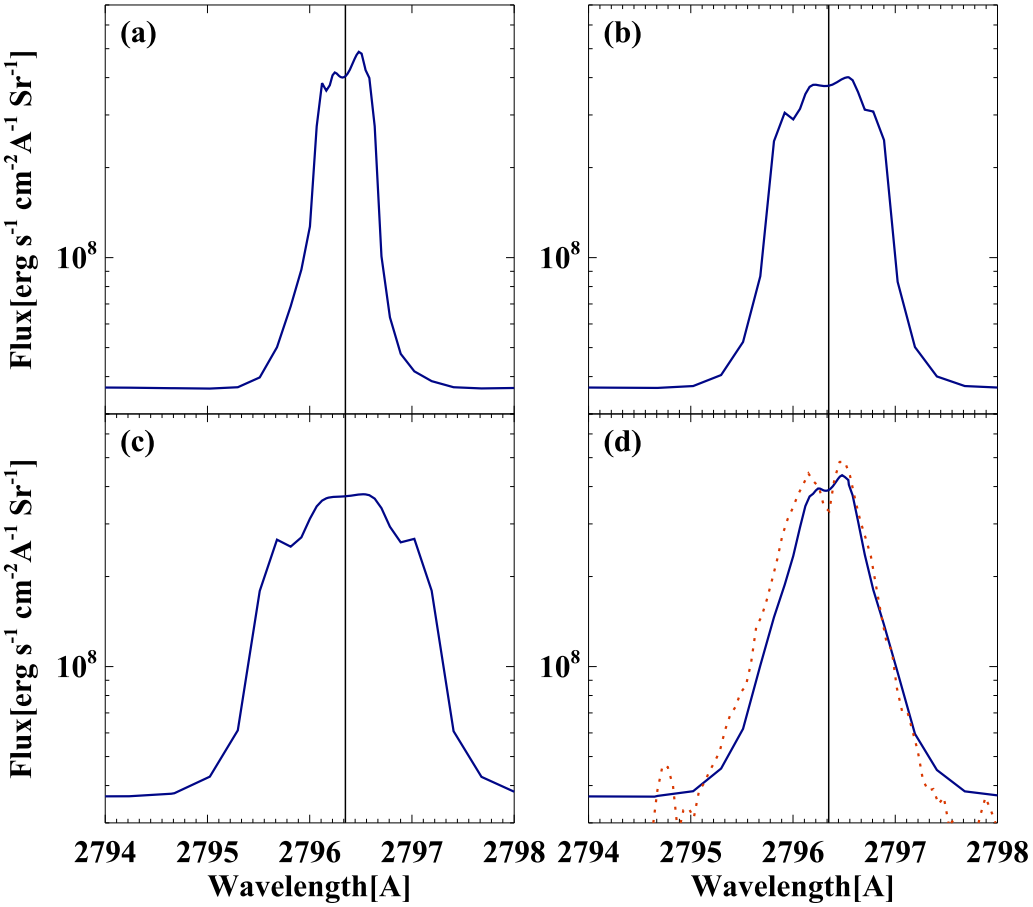

Figure 4. Mg II k profiles with different microturbulence velocities at 10, 20, 30 km s^{-1} in panels (a)–(c) respectively. Panel (d): the solid blue curve shows the synthetic line profile from the simulation, and the observed profile is shown in dotted red curve.

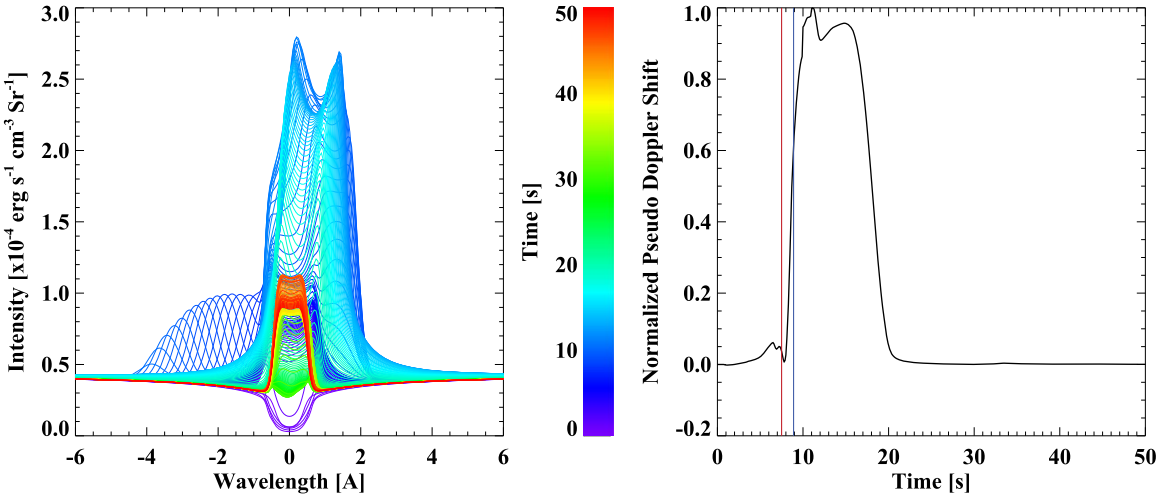

Figure 5. Left panel: Hα spectral profiles produced by RADYN at different time, which is shown in the color bar. Right panel: normalized pseudo-Doppler shift of Hα $\pm$ 1.0 Å. The red and blue vertical lines are marking the timing corresponding to the red and blue plots in Figure 3, at $t = 7.5$ s and $t = 8.9$ s respectively.

The calculated emission is about an order of magnitude higher than that in previous studies, such as Rubio da Costa et al. (2016). A possible cause is the small flaring area derived using high spatial observations. This leads to a relatively higher energy flux of electrons, which is one of the key inputs of RADYN. Note that the background emission also increased proportionally, therefore the normalized line profile is still valuable in qualitative analysis.

Kuridze et al. (2015) and Brown et al. (2018) studied different hydrogen lines and showed asymmetries of optically thick lines in flaring atmosphere. Kerr et al. (2016) computed the Mg II k line using wave-heated and beam-heated simulations, and reported a noticeable difference. The line profiles behave in a complicated way, which requires caution. The RH code is time-independent and uses statistical equilibrium, which means that the populations are in equilibrium. Carlsson

& Stein (2002) studied dynamic hydrogen ionization and noted the effect on hydrogen. To archive comprehensive understanding of the modeled spectral profiles, more details of population equilibrium for Mg II lines are needed.

We thank the BBSO and *IRIS* teams for providing the data. The BBSO operation is supported by NJIT, US NSF AGS 1821294, and the GST operation is partly supported by the Korea Astronomy and Space Science Institute and Seoul National University. *IRIS* is a NASA Small Explorer mission developed and operated by LMSAL with mission operations executed at NASA Ames Research center and major contributions to downlink communications funded by the Norwegian Space Center (NSC, Norway) through an ESA PRODEX contract. NJIT. We would like to thank the anonymous referee for the very valuable comments that improved this work. This work is supported by NSF under grants AGS 1408703, 1539791, and 1821294, and by the NASA under grants NNX16AF72G, 80NSSC17K0016, 80NSSC19K0257, and 80NSSC19K0859. V.M.S. is supported by the NASA NESSF grant NNX16AP05H. We especially thank Lucia Kleint for her valuable suggestions and comments.

ORCID iDs

Nengyi Huang https://orcid.org/0000-0001-9049-0653
Viacheslav M Sadykov https://orcid.org/0000-0002-4001-1295
Ju Jing https://orcid.org/0000-0002-8179-3625
Haimin Wang https://orcid.org/0000-0002-5233-565X

References

Allred, J. C., Hawley, S. L., Abbett, W. P., & Carlsson, M. 2005, ApJ, 630, 573
Allred, J. C., Kowalski, A. F., & Carlsson, M. 2015, ApJ, 809, 104
Brown, S. A., Fletcher, L., Kerr, G. S., et al. 2018, ApJ, 862, 59
Canfield, R. C., Penn, M. J., Wulser, J.-P., & Kiplinger, A. L. 1990, ApJ, 363, 318
Carlsson, M., & Stein, R. F. 1992, ApJL, 397, L59
Carlsson, M., & Stein, R. F. 1997, ApJ, 481, 500
Carlsson, M., & Stein, R. F. 2002, ApJ, 572, 626
De Pontieu, B., Title, A. M., Lemen, J., et al. 2014, SoPh, 289, 2733
Ding, M. D., Fang, C., & Huang, Y. R. 1995, SoPh, 158, 81
Falchi, A., Qiu, J., & Cauzzi, G. 1997, A&A, 328, 371
Fisher, G. H., Canfield, R. C., & McClymont, A. N. 1985, ApJ, 289, 425
Goode, P. R., & Cao, W. 2012, in ASP Conf. Ser. 463, Second ATST-EAST Meeting: Magnetic Fields from the Photosphere to the Corona, ed. T. R. Rimmele et al. (San Francisco, CA: ASP), 357
Graham, D. R., & Cauzzi, G. 2015, ApJL, 807, L22
Graham, D. R., Fletcher, L., & Hannah, I. G. 2011, A&A, 532, A27
Harrison, R. A., Sawyer, E. C., Carter, M. K., et al. 1995, SoPh, 162, 233
Huang, N., Xu, Y., & Wang, H. 2018, RNAAS, 2, 7
Isobe, H., Kubo, M., Minoshima, T., et al. 2007, PASJ, 59, 807
Jing, J., Liu, R., Cheung, M. C. M., et al. 2017, ApJL, 842, L18
Jing, J., Xu, Y., Cao, W., et al. 2016, NatSR, 6, 24319
Kerr, G. S., Fletcher, L., Russell, A. e. J. B., & Allred, J. C. 2016, ApJ, 827, 101
Kuridze, D., Mathioudakis, M., Simões, P. J. A., et al. 2015, ApJ, 813, 125
Leenaarts, J., Pereira, T. M. D., Carlsson, M., Uitenbroek, H., & De Pontieu, B. 2013, ApJ, 772, 90
Lemen, J. R., Title, A. M., Akin, D. J., et al. 2012, SoPh, 275, 17
Lin, R. P., Dennis, B. R., Hurford, G. J., et al. 2002, SoPh, 210, 3
Milligan, R. O. 2015, SoPh, 290, 3399
Panos, B., Kleint, L., Huwyler, C., et al. 2018, ApJ, 861, 62
Pesnell, W. D., Thompson, B. J., & Chamberlin, P. C. 2012, SoPh, 275, 3
Rubio da Costa, F., & Kleint, L. 2017, ApJ, 842, 82
Rubio da Costa, F., Kleint, L., Petrosian, V., et al. 2016, ApJ, 827, 38
Sharykin, I. N., & Kosovichev, A. G. 2014, ApJL, 788, L18
Sukhorukov, A. V., & Leenaarts, J. 2017, A&A, 597, A46
Tei, A., Sakaue, T., Okamoto, T. J., et al. 2018, PASJ, 70, 100
Tian, H., DeLuca, E. E., Cranmer, S. R., et al. 2014, Sci, 346, 1255711
Uitenbroek, H. 2001, ApJ, 557, 389
Wang, H., Chae, J., Gurman, J. B., & Kucera, T. A. 1998, SoPh, 183, 91
Wang, H., Liu, C., Ahn, K., et al. 2017, NatAs, 1, 0085, EP
Xu, Y., Cao, W., Ding, M., et al. 2016, ApJ, 819, 89
Xu, Y., Cao, W., Liu, C., et al. 2006, ApJ, 641, 1210